ically, we showed that blood vessel endothelium induces endocrine pancreatic differentiation. Taken together with previous embryological work (*14, 16*), these data indicate that prepancreatic endoderm is patterned in a stepwise manner, beginning with signals from the mesoderm/ectoderm at 7.5 dpc (*14*), followed by signals from the notochord during the next day (*16*). The blood vessel endothelium then provides the prepatterned endoderm with additional signals that induce differentiation of insulin-expressing cells. The fact that early endoderm, including the prepancreatic region, expresses VEGF (*4*) could explain how the vessels are attracted to the growing pancreas and islets. In a broader context, our data suggest that the close physiological relationship between blood vessels and islets in the pancreas depends on inductive interactions that begin at the earliest stages of development. This type of mutual signaling between tissues and blood vessels during development may be a general mechanism used in vertebrate organogenesis.

References and Notes

1. G. H. Fong, J. Rossant, M. Gertsenstein, M. L. Breitman, *Nature* **376**, 66 (1995).
2. F. Shalaby *et al.*, *Nature* **376**, 62 (1995).
3. N. Ferrara, *J. Mol. Med.* **77**, 527 (1999).
4. D. J. Dumont *et al.*, *Dev. Dyn.* **203**, 80 (1995).
5. P. Carmeliet *et al.*, *Nature* **380**, 435 (1996).
6. N. Ferrara *et al.*, *Nature* **380**, 439 (1996).
7. F. G. Banting, C. H. Best, *J. Lab. Clin. Med.* **115**, 254 (1990).
8. J. Jonsson, L. Carlsson, T. Edlund, H. Edlund, *Nature* **371**, 606 (1994).
9. M. F. Offield *et al.*, *Development* **122**, 983 (1996).
10. Supplementary Web material is available at *Science* Online at www.sciencemag.org/cgi/content/full/1064344/DC1
11. Mouse pancreatic development is initially symmetric (Fig. 1, A through G, and Fig. 5A) with three buds forming adjacent to the dorsal aorta and the two vitelline veins. This is also seen in frog embryos, where the dorsal bud contacts the dorsal aorta, and each ventral bud is adjacent to a vitelline vein plexus (*22*). In mice, we observed that only one of the two ventral pancreatic buds develops into pancreatic tissue, whereas the other bud regresses, coinciding with a developing asymmetry of vitelline veins. The ventral bud adjacent to the endothelium of the right vitelline (portal) vein continues to grow and develop, whereas the left ventral bud disappears together with the left vitelline vein.
12. G. Christofori, P. Naik, D. Hanahan, *Mol. Endocrinol.* **9**, 1760 (1995).
13. G. Teitelman, J. Lee, D. J. Reis, *Dev. Biol.* **120**, 425 (1987).
14. J. M. Wells, D. A. Melton, *Development* **127**, 1563 (2000).
15. Aortic endothelium is removed at 8.25 to 8.5 dpc, a stage when endothelial cells have just recently coalesced into tubes and when supporting mural cells have not yet started to envelop the endothelium of the blood vessels. To ensure isolation of purified endothelium, we used enzymatic treatment to remove any adhering mesenchymal cells (*10*).
16. S. K. Kim, M. Hebrok, D. A. Melton, *Development* **124**, 4243 (1997).
17. There are two possible explanations for the difference in insulin expression induced by the notochord in chick and mouse endodermal explants. There may be a fundamental mechanistic difference between chick and mouse. However, we favor the possibility that chick endodermal explants may have contained contaminating endothelial cells. Endothelial tissues are pervasive and difficult to detect at early stages of chick development. Without enzymatic treatment to eliminate adhering endothelium or specific assays to detect endothelial cells, it is difficult to rule out contamination.
18. O. Cleaver, P. A. Krieg, *Development* **125**, 3905 (1998).
19. During the removal of the intermediate mesoderm, damage to the underlying endoderm results in immediate extrusion of yolky cellular material from the large endodermal cells. Any embryo incurring such damage was identifiable and immediately discarded (*10*).
20. J. E. Lee *et al.*, *Science* **268**, 836 (1995).
21. N. Hirsch, W. A. Harris, *J. Neurobiol.* **32**, 45 (1997).
22. O. G. Kelly, D. A. Melton, *Dev. Dyn.* **218**, 615 (2000).
23. A. Ruiz, I. Altaba, C. Cox, T. M. Jessel, A. Klar, *Proc. Natl. Acad. Sci. U.S.A.* **90**, 8268 (1993).
24. C. S. Newman, F. Chia, P. A. Krieg, *Mech. Dev.* **66**, 83 (1997).
25. A total of 11 fluorescent *Pdx-VEGF* animals derived from independent microinjections were analyzed (five at 15.5 dpc, five at birth, and one stable line). Five of five fluorescent neonates displayed a hyperplastic distribution of islets at birth. To rule out nonspecific effects of *Pdx1*-driven EGFP, a transgene driving only *IRES-EGFP* under the *Pdx1* promoter was used. Three of three fluorescent *Pdx-EGFP* transgenic mice had a normal distribution of insulin expressing islets and amylase expressing acini.
26. K. L. Wu *et al.*, *Mol. Cell. Biol.* **17**, 6002 (1997).
27. It is likely that islet hyperplasia in transgenics is caused by an increased number of blood vessels rather than a direct effect of VEGF on pancreatic epithelium. Two different anti-VEGFR2 antibodies stain blood vessels, but not pancreatic epithelial cells, suggesting that the latter tissue cannot respond directly to VEGF. Our results agree with a study showing VEGF receptor expression in capillary endothelium within the pancreas (*12*).
28. E. Lammert, J. Brown, D. A. Melton, *Mech. Dev.* **94**, 199 (2000).
29. R. A. Brekken, X. Huang, S. W. King, P. E. Thorpe, *Cancer Res.* **58**, 1952 (1998).

30. We thank J. Dubauskaite for the production of transgenic mice. We are grateful to R. Brekken, C. V. Wright, A. Nagy, and P. A. Krieg for essential reagents (*10*). We also thank A. P. McMahon, P. A. Krieg, Y. Dor, J. Wells, A. Grapin-Botton, L. Murtaugh, and T. Carroll for critical comments. E.L. was supported by the Deutsche Forschungsgemeinschaft (La 1216/1-1) and is currently supported by the American Diabetes Association, O.C. is supported by the Cancer Research Fund of the Damon Runyon–Walter Winchell Foundation Fellowship (DRG 1534), and D.M. is an investigator of the Howard Hughes Medical Institute.

12 July 2000; accepted 12 September 2001
Published online 27 September 2001;
10.1126/science.1064344
Include this information when citing this paper.

REPORTS

Charge Migration in DNA: Ion-Gated Transport

Robert N. Barnett,[1] Charles L. Cleveland,[1] Abraham Joy,[2] Uzi Landman,[1]* Gary B. Schuster[2]*

Electron hole (radical cation) migration in DNA, where the quantum transport of an injected charge is gated in a correlated manner by the thermal motions of the hydrated counterions, is described here. Classical molecular dynamics simulations in conjunction with large-scale first-principles electronic structure calculations reveal that different counterion configurations lead to formation of states characterized by varying spatial distributions and degrees of charge localization. Stochastic dynamic fluctuations between such ionic configurations can induce correlated changes in the spatial distribution of the hole, with concomitant transport along the DNA double helix. Comparative ultraviolet light–induced cleavage experiments on native B DNA oligomers and on ones modified to contain counterion (Na^+)-starved bridges between damage-susceptible hole-trapping sites called GG steps show in the latter a reduction in damage at the distal step. This reduction indicates a reduced mobility of the hole across the modified bridge as predicted theoretically.

Recent experiments have established that hole (radical cation) transport occurs in DNA to distant sites (*1–4*), and these results have led to speculation that trapping sites evolved to protect genomic DNA from oxidative reactions (*5*). Long-range charge transport in DNA is being assessed for application to nanoelectronic technologies (*6*), and intensive research has been aimed at elucidation of the energetics and dynamics of charge migration in DNA (*7*) both in vivo, (*8, 9*) and in solution (*1–4, 10*).

Exploration of charge transport in DNA has focused on studies of synthetic oligomers labeled with redox probes that are initiated by photochemical or electrochemical techniques and assessed by spectroscopic or chemical methods (*1–4, 11*). These efforts were designed to elucidate the factors that control the elementary steps of charge injection, transport, and trapping to test their dependencies on base-sequence, in particular, and to test theoretical models centered on phenomenological kinetic schemes (*12–14*). Transport models include (i) A coherent single-step tun-

[1]School of Physics, [2]School of Chemistry and Biochemistry, Georgia Institute of Technology, Atlanta, GA 30332, USA.

*To whom correspondence should be addressed. E-mail: uzi.landman@physics.gatech.edu (U.L.); gary.schuster@cos.gatech.edu (G.B.S.)

neling process between states localized on initial and final sites, yielding an exponential fall off of the tunneling probability with distance. (ii) An incoherent random-walk multistep hopping process (*12*) between initial and final sites, where hops between sequential G bases along the path (acting as hole "resting-sites") are mediated by superexchange involving coupling of states on the G bases with virtual states of the intervening (A/T) sequences ("bridges"). This multistep hopping leads to a weaker fall off of the tunneling probability with distance between the initial and final sites and an algebraic decrease with the number of bridges (*15–17*). And (iii), a long-range polaron-like hopping process (*18*) in which local energy-lowering dynamic structural distortions lead to the formation of a "distortion-dressed" self-trapped state with a finite spatial extent. In this process, superexchange is not invoked and long-range charge transport occurs through a sequence of thermal hopping events that transfer the polaron from one location to another through true charged chemical intermediates that reside on the bridge.

DNA and its environment form a polyelectrolytic heterogeneous medium with interaction potentials of variable strength and spatial range, including covalent, ionic, and hydrogen bonding; dispersion; and multipolar electrostatic interactions. The challenge of gaining fundamental insight into charge transport in DNA is compounded by the dynamically complex nature of DNA and its environment. Dynamical processes range from vibrations with periods as short as tens of femtoseconds to a broad spectrum of diffusive motions (of the counterions and water molecules) that evolve on time scales between tens to hundreds of picoseconds (*19*, *20*). We find that these energetic, structural, and dynamic factors of DNA and its environment substantially influence the charge transport mechanism in DNA and limit the validity and applicability of treatments that do not explicitly incorporate these effects.

We report results obtained by large-scale, first-principles quantum-mechanical simulations (*21–26*) of native and oxidized (by removal of one electron) configurations of a 4–base pair (bp) B-DNA duplex d(5′-$G_1A_2G_3G_4$-3′) with an intact sugar-phosphate backbone, and including the neutralizing Na^+ counterions and a hydration shell. The oligomer was chosen because it is composed of the principal components often considered in studies of charge transport in DNA (e.g., G, GG, and a bridging A). Quantum calculations were performed on configurations that were selected from independent room temperature classical molecular dynamics (MD) simulations and distinguished from each other by the locations of the counterions and hydrating molecules (*27–29*). From such studies, we conclude that inclusion of the sugar-phosphate backbone, of the counterions, and of the solvating water is essential for a proper and accurate description of the energetics and dynamics of charge transport in DNA [for illustrative comparative studies, see the supplemental material (*30*)]. Moreover, the ionization potentials that govern the enthalpic driving forces for charge transport and the spatial distribution of the transported charge (i.e., the hole) depend on the dynamically evolving configurations of the counterions and the solvating water molecules. Of particular importance are configurations (Fig. 1) in which the Na^+ counterions populate backbone sites (i.e., in the vicinity of the negatively charged phosphates) and those in which some of the counterions reside in the grooves of the DNA helix (mainly near the electronegative atoms; e.g., N7 of guanine and adenine) (*21*, *31*).

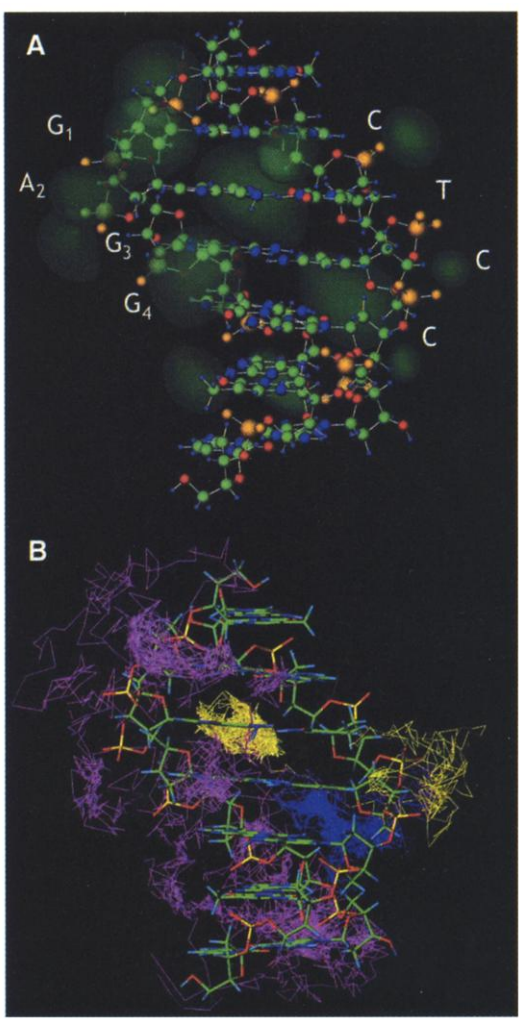

Fig. 1. Results from room-temperature classical molecular dynamics simulations of the 7-bp duplex d(5′-$AG_1A_2G_3G_4AG$-3′). The quantum-mechanical calculations discussed in the text were performed for the 4-bp segment d(5′-$G_1A_2G_3G_4$-3′); the identity of the bases in the 4-bp segment is indicated in the upper panel. (**A**) Counterion (Na^+) probability distribution isosurfaces (Na^+ "visitation map") superimposed (green) on the atomic configuration of the duplex, with the atoms represented by spheres (with corresponding ionic radii) distinguished by color as follows: carbon, green; nitrogen, blue; phosphorous, larger yellow sphere; oxygens of the bases or sugars, red, and those of the phosphate groups, smaller yellow spheres; and hydrogens, (smallest blue spheres). The solvating water molecules are not shown. The isosurfaces, which were obtained through analysis of MD simulations of 1.4-ns duration, give a visual representation of the spatial distribution of regions with high probability for finding the counterions. (**B**) Three representative 1.4-ns trajectories (differentiated by color) of Na^+ countrerions, superimposed on the atomic structure of the duplex (depicted for clarity with the use of a "stick-bonds" representation).

From these findings, a microscopic mechanism of hole transport in DNA emerges in which the (quantum) hole migration is gated in a correlated manner by the finite-temperature (configurational) dynamics of the hydrated counterions. In this "ion-gated transport" (IGT) mechanism, only a small fraction of the thermally accessible ionic configurations contribute to the spatial movement of the hole, with the basin of attraction (i.e., the catchment basin in the multidimensional phase-space of the system) of such "charge-transport effective configurations" (CT-ECs) being relatively narrow. Thus, the hole may reside in a given location for many dynamically evolving configurations, which we term "charge-transport-ineffective," or CT-ICs, that fluctuate on a relatively short time scale of tens of picoseconds until one of the CT-ECs is reached with concomitant movement of the hole. Therefore, the time scale for the migration of the hole is controlled by the rate of passage through the phase space (energetic and entropic) bottleneck into the CT-ECs, and this time scale may be orders of magnitude longer than the characteristic ion diffusion time in the surrounding hydration medium. This microscopic mechanism is built on classical Marcus electron transfer theory and is related to the more recent study of ion-pairing effects on elec-

tron transfer rates in which dynamical fluctuations of counterion positions modulate donor and acceptor energy levels, enabling the electron transfer reaction (*32*). In the present study, important aspects of the influence of hydrated counterion dynamics on donor, acceptor, and bridge states are revealed for charge transport in DNA.

Results obtained from the quantum simulations for certain selected configurations of the counterions and solvating water molecules are shown in Figs. 2 and 3. These configurations correspond to local potential energy minima, with the Na^+ located in sites with high-occupation probabilities (see counterion "visitation map," Fig. 1A). In each case, the selected configuration (*33*) includes at least the first water solvation shell about the sodium ions and phosphate groups (*34*). The main structural difference between the configurations shown in Figs. 2 and 3 is the location of just one Na^+, with all the others occupying sites in the vicinity of the phosphates. That is, in configuration (I) (Fig. 2), all Na^+ are near the phosphates, thus forming a "coaxial double-layer" about the helix of the (duplex) DNA bases, together with the backbone phosphates. The vertical ionization potential (vIP) of this configuration vIP(I) = 5.22 eV. In configuration (II) (Fig. 3A), however, one Na^+ is displaced to the major groove near the N7 of G3. For this configuration vIP(II) = 5.46 eV. The same configuration (II) but without the solvating water molecules is shown in Fig. 3B. The ionization potential for the dehydrated system is vIP(IIdh) = 4.16 eV; the increase of vIP upon hydration originates from increased electronic binding caused by the solvating water molecules (*35*). Configuration (III) (Fig. 3C) is another "groove configuration" with one Na^+ located near the N7 of G_1 of the duplex. For this configuration, vIP(III)= 5.69 eV.

Certain salient features of the ionization energetics of DNA are observed from inspection of the orbital isosurfaces shown in Fig. 2 for configuration (I), where the Kohn-Sham π-like highest occupied molecular orbital (HOMO) (Fig. 2A) is located on the G_3G_4 pair. After (vertical) ionization, the two orbitals at the top of the electronic energy level spectrum are nearly degenerate and are distributed over the purine strand of the 4–base pair duplex (see Fig. 2, C and D) (*36*). This process delocalizes the hole; see isosurfaces of the total charge difference between the neutral and ionized species (Fig. 2B) with a hole distribution of 20% on G_1, 5% on A_2, 40% on the G_3G_4 pair, and the rest delocalized over the sugar-phosphate backbone and some on the water molecules. The spatial distribution of the hole (Fig. 2B) does not resemble that of the HOMO of the native (neutral) duplex (Fig. 2A).

The hole distribution shown for the radical cation in configuration (II) (Fig. 3A) is similar to that of configuration (I) (Fig. 2B) but with a higher ionization potential [vIP(II) = 5.46 eV]; similar behavior (that is, a delocalized hole-distribution with vIP values fluctuating in the range of 5.35 ± 0.1 eV) is found for several other configurations of the counterions where the Na^+ occupies various sites in the vicinity of the phosphates or with one located in the major groove. From these findings, we postulate that a major portion of the configurational thermal equilibrium en-

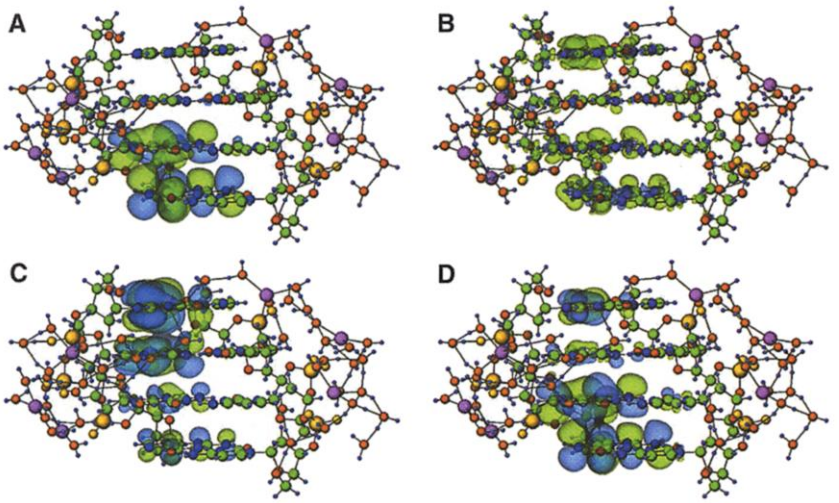

Fig. 2. Results from quantum calculations for the 4-bp duplex d(5′-$G_1A_2G_3G_4$-3′) with all the Na^+ counterions (purple spheres) in the vicinity of the phosphates [configuration (I)]; the geometry of the bases and sugar-phosphate backbone are the same as in Fig. 1. The oxygens of the solvating water molecules are depicted by orange spheres bonded to hydrogens that are represented by small blue spheres; all other colors are assigned as given in Fig. 1A. (**A**) Isosurfaces of the π-like HOMO orbital of the neutral duplex (localized on the G_3G_4 pair); the two different colors of the isosurfaces correspond to the different signs of the wave function. (**B**) Isosurface (green) of the total electron charge density difference between the neutral and ionized duplex, depicting the spatial distribution of the hole that is found to be delocalized over the $G_1A_2G_3G_4$ strand of the duplex. (**C** and **D**) Isosurfaces of the two near-degenerate spin-orbitals at the top of the electronic energy spectrum of the vertically ionized (oxidized) duplex.

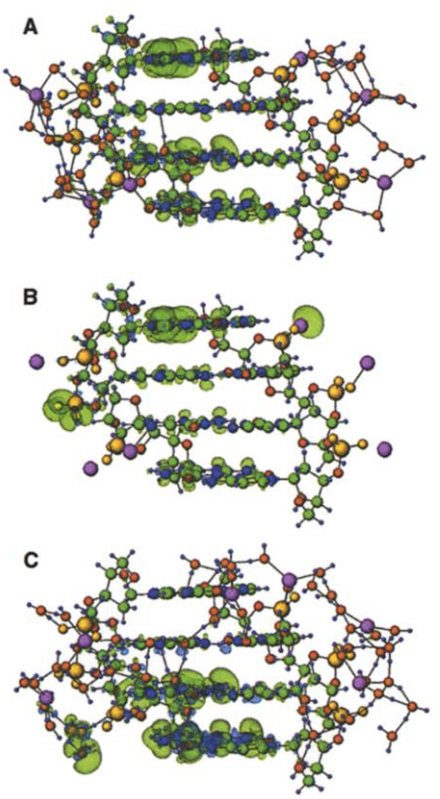

Fig. 3. Isosurfaces of the total electronic charge density differences (shown in green) superimposed on the 4-bp duplex d(5′-$G_1A_2G_3G_4$-3′). The structure of the duplex, including the bases and sugar-phosphate backbone, is the same as in Figs. 1 and 2. (**A** and **B**) Results corresponding to counterion configuration (II), where one of the Na^+ resides in the major groove (in the vicinity of the N7 of G_3) and all other counterions are located in the vicinity of the phosphates. The result in (A) was calculated with the solvating water molecules included and in (B) was calculated for the same geometry but without the hydration shell. Note the significant effect of hydration on the spatial distribution of the hole, and the remarkable similarity between the delocalized hole distribution in the hydrated duplex (A) and the one corresponding to configuration (I) (Fig. 2B, where all Na^+ are in the vicinity of the phosphates). (**C**) Results corresponding to configuration (III), where one of the Na^+ is located near the N7 of G_1. Note the difference between the hole spatial distribution, which is localized on the G_3G_4 pair, and those corresponding to configuration (I) (Fig. 2B) and configuration (II) (A), where the hole is delocalized over the $G_1A_2G_3G_4$ strand. All colors and sphere assignments are the same as in Fig. 2.

semble belongs to the aforementioned CT-IC class. In contrast, a thermal fluctuation that allows the system to access a configuration belonging to the CT-EC class can result in transport of the hole accompanied by hole-localization on the G_3G_4 pair (Fig. 3C) with a marked increase of the vIP [vIP(III) = 5.69 eV]. The total potential energy of this "groove configuration" is higher by 0.2 eV than that of configuration (I) where all the counterions are near the phosphates. Transport of a hole can indeed be achieved via certain configurational fluctuations of the counterions that surmount the free-energy barriers associated with the hole transport and localization process. Such configurational fluctuations cause a random walk of the hole until irreversible trapping occurs by reaction with water.

Because the above ion-gated hole-transport (IGT) process is controlled by the dynamical fluctuations of the arrangements of the counterions (and of the solvating water molecules), the ideas underlying the IGT mechanism can be tested by exploring effects that may be correlated directly with a designed modification of the local counterion concentration at selected segments along the hole-migration path. Such modification can be achieved through replacement of certain phosphate groups with methylphosphonates (PO_3CH_3) because the latter carry no formal charge and, thus, do not have a propensity to attract Na^+ ions [see supplementary material (*30*)]. Indeed, in classical MD simulations with methylphosphonates replacing the backbone phosphates on the A-strand of an $(A)_3$ embedded in the 7-bp duplex d(5′-AGAAAGG-3′), we observed no propensity for the counterions to populate the modified region. Furthermore, quantum calculations for the d(5′-AAA-3′) bridge yielded for the (native) unmodified backbone vIP = 5.90 eV, with 50% of the hole delocalized over the A bases and 20% over the complementary thymines and the rest distributed mainly over the sugar-phosphate backbone and some on the water molecules. For the same duplex but with an $(A)_3$ phosphonated bridge (i.e., no Na^+ on the $(A)_3$ strand but including a hydration shell), we obtained vIP = 6.16 eV, and the hole is distributed 40% on the $(A)_3$ and 25% on the complementary $(T)_3$. The increased ionization potential of the phosphonated $(A)_3$ bridge, together with its aforementioned counterion-starved local environment, is predicted to reduce the probability for transfer of a hole into it. Thus, the modified $(A)_3$ segment may be regarded as a "raised bridge" that inhibits transport through it, and it may instead back-scatter (reflect) an incident hole.

These predictions were tested experimentally by investigation of DNA oligomers covalently linked to an anthraquinone group and containing methylphosphonates between GG steps. Irradiation of the quinone introduces a radical cation into the DNA; reaction of the hole with water at the GG steps (which results in strand cleavage after treatment with *Fpg* protein) (*37*) indicates the efficiency of radical cation transport. Figure 4 shows the results from this experiment with methylphosphonate substitution at the $(A)_3$, the $(T)_3$, or the $(A/T)_3$ segments in the form of a polyacrylamide gel. Substitution of the phosphate groups by methylphosphonates leads to a significant reduction in radical cation migration, which is predominantly an effect of methylphosphonate substitution in the $(A)_3$ segment.

In the IGT mechanism, the transport of a hole from one location to another involves transitions between (quantum mechanical) hole states (which may extend over several DNA bases) characterized by varying degrees of localization that are governed by and correlated with the dynamically evolving local ionic configurations. Thus, the characteristics of the hole-transport process are expected to be temperature-dependent because of the activated nature of the structural transitions involved. Local ionic configurations will likely depend on the specific structure of the DNA, so the transport model should be sensitive to base sequence. However, a strong dependence of the hole-transport efficiency on the identity of the counterions is unlikely, as was found experimentally, (*38*) because the identity of the mono-positve cation should not significantly affect the relative populations of the aforementioned CT-ECs and CT-ICs.

These findings provide a useful conceptual framework and an impetus for further experimental tests of the IGT mechanism and motivate continued theoretical investigations. These may include incorporation of stochastic ion-gating processes in kinetic transport models; calculations of effective electronic couplings between DNA bases with the inclusion of structural fluctuations of the DNA and its hydrated counterion environment, and evaluation of transport rates without factorization into electronic and nuclear (Franck Condon) terms; and finite temperature time-dependent quantum molecular dynamics simulations of ion-gated charge transport in DNA.

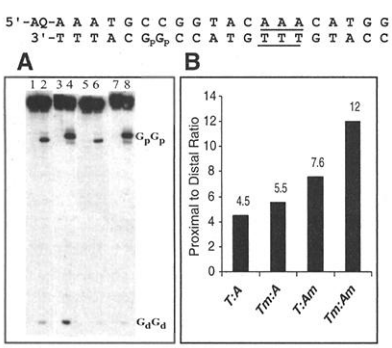

Fig. 4. An autoradiogram of a polyacrylamide gel (**A**) from irradiation [350 nm, only the anthraquinone (AQ) absorbs (*1*)] of the duplex DNA conjugate shown after treatment with *Fpg* protein (*37*), which results in strand cleavage at oxidized guanines. Lanes 1, 3, 5, and 7 are "dark controls" in which the samples were not exposed to ultraviolet light. The experimental results are shown in the corresponding lanes 2, 4, 6, and 8 in which the $(A/T)_3$ sequence (underlined in the structure) contains normal phosphates (lane 2); methylphosphonates linking the T bases (Tm, lane 4); methylphosphonates linking the A bases (Am, lane 6); and methylphosphonates linking both the A and T bases (lane 8). All samples are racemic. Phosphorimagery reveals the relative amount of proximal (G_pG_p) to distal (G_dG_d) cleavage on the ^{32}P-labeled strand, shown in (**B**), which is a measure of the efficiency of radical cation transport across the bridge.

References and Notes

1. G. B. Schuster, *Accts. Chem. Res.* **33**, 253 (2000).
2. B. Giese, *Accts. Chem. Res.* **33**, 631 (2000).
3. C. Z. Wan, T. Fiebig, O. Schiemann, J. K. Barton, A. H. Zewail, *Proc. Natl. Acad. Sci. U.S.A.* **97**, 14052 (2000).
4. F. D. Lewis, R. L. Letsinger, M. R. Waiselewski, *Accts. Chem. Res.* **34**, 159 (2001).
5. A. Heller, *Faraday Discuss.* **116**, 1 (2000).
6. H.-W. Fink, *Cell. Mol. Life Sci.* **58**, 1 (2001).
7. M. A. Ratner, *Proc. Natl. Acad. Sci. U.S.A.* **98**, 387 (2001).
8. D. Wang, D. A. Kreutzer, J. M. Essigmann, *Mutation Res.* **400**, 99 (1998).
9. B. Boudaiffa, P. Cloutier, D. Hunting, M. A. Huels, L. Sanche. *Science* **287**, 1658 (2000).
10. E. Meggers, M. E. Michel-Beyerle, B. Giese, *J. Am. Chem. Soc.* **120**, 12950 (1998).
11. N. M. Jackson, M. G. Hill, *Curr. Opin. Chem. Biol.* **5**, 209 (2001).
12. J. Jortner, M. Bixon, T. Langenbacher, M. E. Michel-Beyerle, *Proc. Natl. Acad. Sci. U.S.A.* **95**, 12759 (1998).
13. Y. A. Berlin, A. L. Burin, M. A. Ratner, *J. Am. Chem. Soc.* **123**, 260 (2001)
14. F. C. Grozema, Y. A. Berlin, L. D. A. Siebbeles, *J. Am. Chem. Soc.* **122**, 10903 (2000).
15. Charge transport models (i) and (ii), described in the text, are built on a foundation of a static hierarchy of base oxidation potentials (GGG < GG < G < A <C,T). This hierarchy, which has been used extensively in kinetic modeling of hole-transport in DNA, is based on data measured for single nucleobases [gas phase ionization potentials (*16*) or oxidation potentials in solution (*17*)], or on estimates obtained from calculations on static crystallographically stacked isolated single-strands or duplexes (two or three bases long). All previous calculations were performed without the sugar-phosphate backbones and hydrated counterion environment. See references to such calculations and comparisons with our values for selected sequences, given in the supplemental material (*30*).
16. N. S. Hush, A. S. Cheung, *Chem. Phys. Lett.* **34**, 11 (1975).
17. S. Steenken, S. V. Jovanovic, *J. Am. Chem. Soc.* **119**, 617 (1997).
18. P. T. Henderson, D. Jones, G. Hampikian, Y. Kan, G. B. Schuster, *Proc. Natl. Acad. Sci. U.S.A.* **96**, 8353 (1999).
19. N. V. Hud, M. Polak, *Curr. Opin. Struct. Biol.* **11**, 292 (2001).
20. D. L. Beveridge, K. J. McConnel, *Curr. Opin. Struct. Biol.* **10**, 182 (2000).
21. The first-principles quantum mechanical calculations were performed using the Born-Oppenheimer (BO) local-spin-density (LSD) MD method [BO-LSD-MD;

for details see (22)], with gradient corrections for the exchange-correlation functional (23). The Kohn-Sham equations were solved in conjunction with norm-conserving nonlocal pseudopotentials for the valence electrons (24) and a plane-wave basis (i.e., no atom-centered basis functions were used) with a high kinetic energy cutoff of 845 eV; a calculation for the 4-bp duplex d(GAGG) with 48 H_2O and 6 Na makes for 1240 valence electrons. The algorithm for solving the density-functional Kohn-Sham equations uses a Fermi distribution function for the electrons, which is a very effective way of dealing with degenerate or near-degenerate energy levels [see (22)]. The Fermi temperature that we used is rather low (0.01 eV/k_B), which assures that the Fermi function is operative only on the near-degenerate levels at the top of the level spectrum and not anywhere else (where the spectral gaps are larger). The BO-LSD-MD method is particularly suitable for calculations of charged systems because no periodic replication of the ions is imposed [that is, no supercells are used; see (22)]. To illustrate the accuracy of the calculations, we give the vertical (v) and adiabatic (a) ionization potentials (IP), calculated for the isolated nucleobases as the total energy difference between the neutral and ionized species. For T, vIP = 8.73 eV, aIP = 8.54 eV; for C, vIP = 8.54 eV, aIP = 8.43 eV; for A, vIP = 8.11 eV, aIP = 7.96 eV; for G, vIP = 7.70 eV, aIP = 7.20 eV. The values obtained from our calculations are consistently lower by 3 to 6% than the measured values (16, 25, 26).

22. R. N. Barnett, U. Landman, *Phys. Rev. B* **48**, 2081 (1993).
23. P. P. Perdew *et al.*, *Phys. Rev. Lett.* **77**, 3865 (1996).
24. N. Troullier, J. J. Martins, *Phys. Rev. B.* **43**, 1993 (1991).
25. V. M. Orlov, A. N. Smirnov, Y. M. Varshvsky, *Tetrahedron Lett.* **48**, 4377 (1976).
26. S. G. Lias, *et al.*, *J. Phys. Chem. Ref. Data* **17** (suppl. 1), 1 (1988).
27. The classical molecular dynamics simulations were performed using the AMBER95 force field with the NWChem package (28). The computational cell contained the 7-bp duplex d(5′-AGAGGAG-3′) (Fig. 1A), which was kept (except for the hydrogens) in its crystallographic structure (29), as well as 12 Na^+ and 840 H_2O, which, together with the DNA hydrogen atoms, were treated dynamically. The dimensions of the Cartesian computational cell were 32 Å by 32 Å by 37 Å, with the larger dimension parallel to the DNA helix axis. The duplex was terminated on both ends by removing the DNA double helix beyond the nearest neighboring P atoms and substituting a hydrogen atom for the removed part. A time step of 1 fs was used throughout, using the velocity Verlet algorithm. The system was equilibrated first at a temperature of 300 K for 200 ps, and phase-space trajectories accumulated for the subsequent 1.4 ns were used in the analysis reported here.
28. High Performance Computational Chemistry Group, *NWChem, A Computational Chemistry Package for Parallel Computers, version 4.0.1*, (Pacific Northwest National Laboratory, Richland, WA, 1998).
29. S. Arnott *et al.*, in *Handbook of Biochemistry and Molecular Biology*, G. D. Fasman, Ed. (CRC Press, Cleveland, 1977), pp. 411–422.
30. Supplementary material is available at *Science* Online at www.sciencemag.org/cgi/content/full/294/5542/567/DC1.
31. L. McFail-Isom, C. C. Sines, L. L. Williams, *Curr. Opin. Struct. Biol.* **9**, 298 (1999).
32. R. Marcus, *J. Phys. Chem. B.* **102**, 10071 (1998)
33. The configurations used in the quantum calculations were extracted from the classical MD simulations. In each case, the configuration was re-optimized to the nearest local potential energy minimum through the use of damped MD. The main effect of this process was to rearrange some of the hydrogen bonds of the outer hydration shell of the selected configuration, and the effect of thermal disorder is maintained. We have verified for a 2-bp duplex d(5′-GG-3′) that quantum mechanical relaxation including the DNA bases, the sugar-phosphate groups, counterions, and water solvation, starting from optimized configurations, do not alter the results in any substantial way.
34. Comparative calculations on a 2-bp duplex d(5′-GG-3′), with sugar-phosphates, counterions and water solvation, have shown that inclusion of water molecules beyond those considered here does not modify the quantum mechanical results in any substantial manner.
35. The higher vIP of the hydrated configuration may, at first, seem surprising in light of the common notion that hydration serves to screen electrostatic interactions and, thus, reduce the effect of the counterions and negatively charged phosphates, whereas the opposite is found here. However, the above screening notion is anchored in bulk (often coarse-grained) considerations, and it does not apply to the interfacial interactions and molecular length scale that characterize the hydration process of DNA. Underlying the increase of the vIP in the hydrated system (that is, stronger binding of the electrons), as well as the marked effect of hydration on the spatial distribution of the hole (compare Fig. 3, A and B), is the preferential orientational ordering of the water molecules in the first (and to a smaller extent in the second) hydration shell, with the enhanced binding originating from the added attractive interaction between the electrons and the dipolar charge distribution of the water molecules.
36. In configuration (I) of the neutral duplex, four orbitals at the top of the occupied electronic manifold form a group separated from the rest of the occupied orbitals by a mini gap (0.52 eV). We denote these orbitals as Ψ_1 (−4.162 eV), Ψ_2 (−4.392 eV), $\Psi 3$ (−4.426 eV), and Ψ_4 (−4.798 eV), in descending order of their energies (with the orbital energies given in parenthesis; i.e., Ψ_1 shown in Fig. 2A is the HOMO). Ψ_1 and Ψ_2 are localized on the G_3G_4 pair, Ψ_3 on G_1, and Ψ_4 on A_2. After ionization, the whole spectrum shifts to lower energies and the above four orbitals mix with each other. The two highest occupied spin-orbitals of the radical cation (shown in Figs. 2C and 2D) are nearly degenerate (with energies of −6.688 eV and −6.703 eV, respectively) and they are delocalized over the 4 base pairs. The occupancies of these spin-orbitals by the lone electron of the ionized duplex are 0.64 and 0.36, respectively. Alternatively, these spin-orbitals may be regarded as the "hole-orbitals" with hole occupancies of 0.36 and 0.64, respectively.
37. J. Tchou *et al.*, *Proc. Natl. Acad. Sci. U.S.A.* **88**, 4690 (1991).
38. Preliminary results from our laboratory show that exchange of Na^+ for K^+ or Li^+ has no measurable effect on the efficiency of charge migration.
39. Supported by the National Science Foundation, the Department of Energy, and the Air Force Office of Scientific Research. Computations were performed on an IBM SP2 computer at the Georgia Tech Center for Computational Material Science and at NERSC, Berkeley, CA.

25 May 2001; accepted 10 September 2001

Reproducible Measurement of Single-Molecule Conductivity

X. D. Cui,[1] A. Primak,[2,3] X. Zarate,[2] J. Tomfohr,[1] O. F. Sankey,[1] A. L. Moore,[2] T. A. Moore,[2] D. Gust,[2] G. Harris,[3] S. M. Lindsay[1]

A reliable method has been developed for making through-bond electrical contacts to molecules. Current-voltage curves are quantized as integer multiples of one fundamental curve, an observation used to identify single-molecule contacts. The resistance of a single octanedithiol molecule was 900 ± 50 megohms, based on measurements on more than 1000 single molecules. In contrast, nonbonded contacts to octanethiol monolayers were at least four orders of magnitude more resistive, less reproducible, and had a different voltage dependence, demonstrating that the measurement of intrinsic molecular properties requires chemically bonded contacts.

Wiring a single molecule into an electrical circuit by chemically bonding each end to a metal conductor is a key requirement for molecule-based electronics. Although conceptually simple, this goal has proven elusive. The variety of methods for contacting molecules includes bonding dithiolated molecules into break junctions (*1*), dipping nanotubes into a mercury pool (*2*), touching molecules in an insulating matrix with a conducting atomic force microscope (AFM) (*3*), using a scanning tunneling microscope (STM) to connect to gold particles attached to dithiolated monolayers (*4*, *5*), and contacting two monolayers together with a mercury-drop electrode (*6*). These pioneering experiments have demonstrated that unambiguous contact to a single molecule is difficult to achieve, as shown by large disparities in conductivities reported for identical (*7*, *8*) or similar (*1*, *9*) molecules. Measured currents can be very sensitive to applied stress (*3*, *10*, *11*), and calculated conductivity can disagree with experimental results by several orders of magnitude (*12*). In many cases, electrical connections to the molecules have been made via nonbonded mechanical contacts rather than chemical bonds, and it is likely that this may account for some of the discrepancies.

Here we report a reliable method for chemically bonding metal contacts to either end of an isolated molecule and measuring the current-voltage $I(V)$ characteristics of the resulting circuit. Molecules of 1,8-octanedithiol were inserted into an octanethiol monolayer [on Au(111)] using a replacement reaction (*13*) whereby one of the two thiol groups becomes chemically bound to the gold substrate (*14*–*17*). The octanethiol monolayer

[1]Department of Physics and Astronomy, [2]Department of Chemistry and Biochemistry, Arizona State University, Tempe, AZ 85287, USA. [3]Motorola, 2100 East Elliot Road, AZ34/EL 704, Tempe, AZ 85284, USA.